Naval Research Laboratory

Washington, DC 20375-5320

NRL/7680/MR--2021/1

Impact of Solar Wind Variability on CME Structure and Propagation

Phillip Hess

Robin Colaninno

Russell Howard Retired

Solar and Heliospheric Physics Branch
Space Science Division

February 5, 2021

REPORT DOCUMENTATION PAGE

Form Approved
OMB No. 0704-0188

1. REPORT DATE (DD-MM-YYYY)	2. REPORT TYPE	3. DATES COVERED (From - To)
05-02-2021	NRL Memorandum Report	10/01/2018 – 09/30/2019

4. TITLE AND SUBTITLE

Impact of Solar Wind Variability on CME Structure and Propagation

5a. CONTRACT NUMBER

5b. GRANT NUMBER

5c. PROGRAM ELEMENT NUMBER
NISE

6. AUTHOR(S)

Phillip Hess, Robin Colannio, and Russell Howard*

5d. PROJECT NUMBER

5e. TASK NUMBER

5f. WORK UNIT NUMBER
N2R4

7. PERFORMING ORGANIZATION NAME(S) AND ADDRESS(ES)

Naval Research Laboratory
4555 Overlook Avenue, SW
Washington, DC 20375-5320

8. PERFORMING ORGANIZATION REPORT NUMBER

NRL/7680/MR--2021/1

9. SPONSORING / MONITORING AGENCY NAME(S) AND ADDRESS(ES)

Naval Research Laboratory
4555 Overlook Avenue, SW
Washington, DC 20375-5320

10. SPONSOR / MONITOR'S ACRONYM(S)

NRL-NISE

11. SPONSOR / MONITOR'S REPORT NUMBER(S)

12. DISTRIBUTION / AVAILABILITY STATEMENT

DISTRIBUTION STATEMENT A: Approved for public release; distribution is unlimited.

13. SUPPLEMENTARY NOTES

Karles Fellowship
*Retired

14. ABSTRACT

We have attempted to improve upon the measurement and theoretical understanding of CMEs in two ways. First, we have used data from the previous solar cycle with improved and unique processing to attempt to improve our understanding of how a CME structure evolves in the heliosphere. We have also used new data from a recently launched satellite, NASA's Parker Solar Probe, to utilize observations that have never before been possible to prepare for the events that will be occurring in the upcoming cycle. By improving our ability to interpret prior data while still preparing for the new data we will receive, we can maximize the the science return that of our missions in the upcoming solar cycle.

15. SUBJECT TERMS

16. SECURITY CLASSIFICATION OF: a. REPORT	b. ABSTRACT	c. THIS PAGE	17. LIMITATION OF ABSTRACT	18. NUMBER OF PAGES	19a. NAME OF RESPONSIBLE PERSON
					Phillip Hess
Unclassified Unlimited	Unclassified Unlimited	Unclassified Unlimited	Unclassified Unlimited	28	19b. TELEPHONE NUMBER (include area code) (202) 767-6942

Standard Form 298 (Rev. 8-98)
Prescribed by ANSI Std. Z39.18

This page intentionally left blank.

CONTENTS

FIGURES

EXECUTIVE SUMMARY

This report presents research conducted by Hess et al. under his Karles Fellowship at NRL, work which is ongoing. The work of this report concerns coronal mass ejections (CMEs), which are significant drivers of space weather. Space weather impacts can cause noticeable impacts on satellites, Navy communications systems and radar. Ultimately, understanding the physical processes which govern CME evolution in the heliosphere can lead to better operational forecasting and improved situational awareness, allowing for the mitigation of negative consequences. This work therefore addresses the goals of the DoD Space S&T Strategic Plan.

We have advanced the measurement and theoretical understanding of CMEs in two ways. First, we have developed and implemented a new image processing technique and used data from the previous solar cycle to improve our understanding of how CME structure evolves in the heliosphere. Specifically, our focus was on the degree to which a CME propagates as a coherent bulk structure as it interacts with the solar wind. We have also used new data from a recently launched satellite, NASA's Parker Solar Probe, to utilize observations that have never before been possible to prepare for the events that will be occurring in the upcoming cycle. The satellite, using a unique elliptical orbit to get closer to the Sun than any mission before, has allowed us to image in great detail smaller eruptions that likely comprise a signification amount of the solar wind. While seemingly weak and insignificant, we have learned that these blobs erupt regularly and contribute significantly to the solar wind. As a proof of concept demonstration of the level of analysis now capable with PSP observations, we can now begin to answer key questions on solar wind formation and CME evolution in the heliopshere. By improving our ability to interpret prior data while still preparing for the new data we will receive, we can maximize the science return of our missions in the upcoming solar cycle.

This page
intentionally
left blank

IMPACT OF SOLAR WIND VARIABILITY ON CME STRUCTURE AND PROPAGATION

1. INTRODUCTION

1.1 Observing the Heliosphere in White-Light

White-light observations of the solar corona date back to the 1970's, with missions such as OSO-7 [47], Skylab [28], the Solar Maximum Mission (SMM) [29], and P78-1 (Solwind) [38].

For the last two decades, consistent imaging of the corona has been done by the Large Angle Spectrometric Coronagraph (LASCO) [7] from near the Sun-Earth line on-board the *Solar and Heliospheric Observatory (SOHO)*. The Sun Earth Coronal Connection and Heliospheric Investigation (SECCHI) [20] on board the twin *STEREO* spacecraft provided the first regular observations of the heliosphere from large angles away from the Earth, though still near 1 AU. In 2018, the Wide-Field Imager for Solar Probe (WISPR [50]) on-board the Parker Solar Probe (*PSP*) [13] became the first instrument to image the solar corona in white-light within 0.3 AU, inside the orbit of Mercury [21].

As white-light instruments, WISPR, SECCHI and LASCO observe a combination of the stable, dust-based F-corona [44] and the dynamic K-corona, consisting of photons scattered by electrons and comprised largely of solar outflows and transients that can impact the Earth [22].

1.2 Coronal Mass Ejections

Coronal mass ejections (CMEs), originally discovered with the NRL coronagraph on OSO-7 in Dec. 1971, are eruptions of magnetized plasma from the low corona, and are among the most notable and well studied solar transients because of the geomagnetic impacts they can cause at the Earth ([52] and references therein). CMEs are of significant interest to the heliophysics community. As major drivers of space weather at the Earth, a comprehensive understanding of how CMEs propagate is vital for real time forecasting.

While well observed from the Earth perspective, multiple viewpoint observations of CMEs only became routinely available after the launch of *STEREO* in 2006. These observations of the solar corona, in combination with the observation from *SOHO* LASCO, helped solidify our current understanding of CMEs as a coherent magnetic structure that can be well represented with the geometry of a flux rope. CMEs have a large range of observed sizes, speeds and energies and one of the key remaining questions in heliophysics is whether all the observed events exist within a continuum undergoing the same physical processes or if there are discrete classifications of events based on how specifically the eruption begins and its size. Studying a large, diverse subset of CMEs is vital for determining our ability to consistently model all events, and not just those that are more easily observed.

Numerous models have been developed and tested to predict when a CME will impact the Earth. However, the performance of these models has stagnated, with an average error on the order of 6-10 hours and an

Manuscript approved February 3, 2021.

even larger standard deviation as the most common performance metrics [36]. Additionally, for events with even a slight deviation from the Sun-Earth line, many models struggle to predict whether or a CME will even impact the Earth at a better than 50/50 rate [53]. Without improving the underlying physics in both theoretical and operational models, the forecasting of space weather will remain limited.

1.3 CME Structure

CMEs in the heliosphere have long been considered to be magnetic flux ropes [49, 56] consisting of helically twisted field lines along a strong central current. Near the Sun, the internal magnetic field of the CME is both what maintains the structure as it propagates and causes it to expand, as the ambient solar wind density around the CME decreases with distance and creates a pressure imbalance. However, in the heliosphere, the degree to which the magnetic structure is maintained is a new avenue of inquiry with broad implications. A limited number of studies have been made into the overall shape of CMEs throughout the heliosphere using remote sensing data. Those that have been performed present compelling observations that indicate the CME undergoes pronounced morphological changes in the transport through the corona to 1 AU [12].

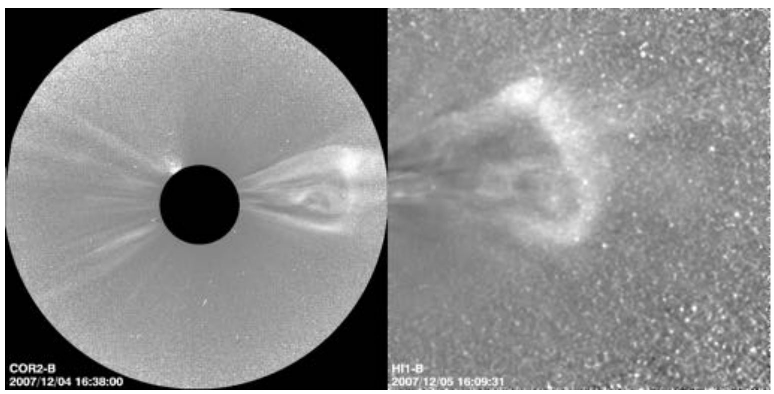

Fig. 1—SECCHI images from COR2-B and HI1-B of the same CME about a day apart, illustrating the observed structural evolution. Out to the edge of COR2, the CME appears to have the classic flux rope shape with a rounded front and interior cavity. In HI1, the front has flattened and the interior cavity has lost definition. The morphological changes with height could indicate a loss of coherence in the magnetic field but instrumental and observational effects between instruments must be mitigated.

Owens et al. [32] presented a theoretical argument that CMEs in the heliosphere cannot be coherent structures and should therefore be treated as a number of unrelated plasma blobs, travelling through the solar wind like particles in a cloud. If this is true, any attempt to impose a geometric structure upon a CME beyond the corona will significantly over simplify the driving physical interactions.

An example of a CME crossing from the SECCHI COR2 ($\sim$4-16 $R_{\odot}$) FOV into HI1 ($\sim$15-80 $R_{\odot}$) from *STEREO*-B is shown in Figure1 in images taken about a day apart. The CME maintains a similar shape, but there are identifiable sub-structures (the bright feature on top of the CME and the more complex, circular feature on the bottom) that have to some degree propagated independently of one another. It also appears as though the front has become less rounded at larger distances. This characteristic flattening of the CME is often observed and referred to as ”pancaking” [35].

In-situ observations of CMEs show signatures indicative of flux ropes, however, this association is only clear in about one third of all events [14]. The *in-situ* signatures can be complex and difficult to interpret, even in events where the association between the CME near the Sun and the *in-situ* observations is obvious [18]. Differences between these two types of observations is often taken as a sign that the *in-situ* spacecraft is flying through the CME far from the nose [8, 23], though this cannot always be proven. Moreover, the difficulty in generating agreement between different *in-situ* reconstruction codes run on the same event [1], as well as, the differences in the few events that were observed *in-situ* by multiple spacecraft [27] raise questions about whether CMEs at 1 AU maintain a flux rope structure [2].

2. CME MEASUREMENT

2.1 The Graduated Cylindrical Shell Model

To study CMEs in the heliopshere, we can use the various observations to generate spatial information of the CME with respect to disntance and time. However, determining the physical position of a CME is not a trivial task. Even if the same event is observed from different perspectives by different spacecraft, this still presents limited data from which to infer the spatial extent of the CME. When all the available data is used to locate the position of the CME, assumptions must be made to combine all the geometric information and provide a common shape that explains all the observations. This task is commonly done by utilizing a geometric model representing a flux-rope like shape imposed on the multiple viewpoint images. A limited number of free parameters representing the size, shape and position of the CME are then adjusted until the shape of the model overlaps with the signal in the imaging data.

The Graduated Cylindrical Shell (GCS) model [45, 46] uses a series of concentric circular cross sections, connected to the Sun by two conic legs, to describe the CME geometry. The GCS shape has become one of the most widely used tools in CME research and has been used to probe the physical forces acting on propagating CMEs [11, 33, 34] and to generate inputs for various forecasting models, both operational and hypothetical [3, 17, 30, 41]. While it can be used on data from a single viewpoint, multiple spacecraft are required to uniquely constrain the observations.

The primary drawback of applying the GCS model to CMEs in the heliosphere is it assumes a constant, self-similar expansion as the CME propagates. While this assumption is valid closer to the Sun, at larger heights it becomes obvious that the GCS shape no longer matches the observations, as demonstrated in figure 2. While the model can be tweaked to match the data as the CME continues to evolve, the model parameters from frame to frame must be consistent to some degree in order to possess physical meaning. Similar to the GCS, Wood and Howard [54] uses a more complex model of a flux-rope like shape with more free parameters to improve the accuracy of the reconstruction.

Regardless of the extra parameters, all of these 3D reconstructions will be limited by their rigidity. These models ignore that in the heliosphere CMEs are complex magnetic ejecta propagating into a variable solar wind. While using a solid body approximation to determine a location and size may be accurate enough to provide reasonable inputs for forecasters, it will not allow for the physical processes of CME evolution to be probed in any detail.

Furthermore, if a kinematic model of CME propagation is using a single height as determined by the GCS, CME propagation is essentially being reduced to a point mass in a 1D problem. While this may be useful to estimate the bulk motion of the plasma, such a method will be unable to capture any inhomogenuities in the mass distribution that can manifest during propagation of internal structures. Additionally, a single

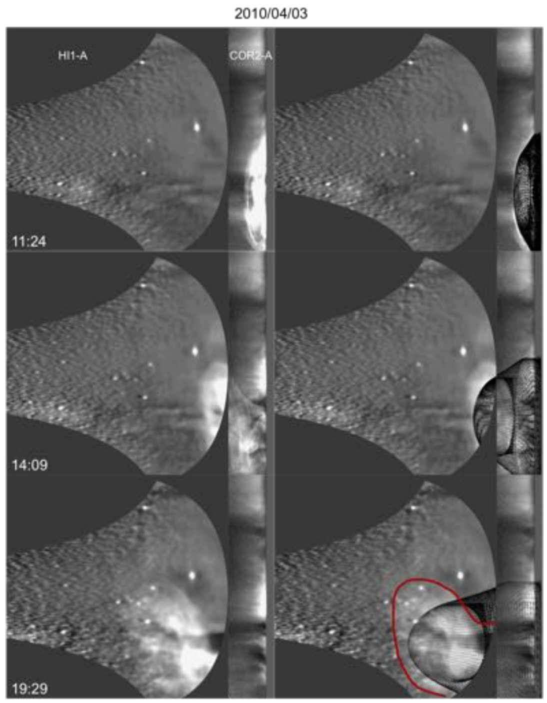

Fig. 2—A GCS fitting along with data from a CME observed 2010-Apr-03 by SECCHI-A. The images are projected onto a rectangular coordinate system, with a linear elongation from the Sun on the x-axis and position angle in the instrument reference on the y-axis. This projection allows COR2 and HI1 images to be combined into a single common field of view. The difference between the model and the data rises sharply as the CME leaves the low corona. In addition to the deviations along the CME front caused by the simplistic rigidity of the model (red line), there is more complicated physics going on behind the CME, where a clear trailing edge is forming and the legs of the ejecta remain narrow.

characteristic upstream solar wind is imposed by such a method, leaving the effect of any external gradient influencing the motion or expansion of the CME completely unresolved.

For these reasons, an ability to determine spatial information about a CME, both at different latitudes and different heights within the CME itself, is vital for determining the structural evolution of a CME as it propagates. This can provide crucial information and help us address the issue of CME structural coherence, as well as improve forecasting models by studying the entire CME rather than just focusing on one specific point along the leading edge.

2.2 Using Density to Infer Structure

Observations from the lower corona SECCHI COR2 and LASCO instruments can be used to understand the deformation of the CME from an idealized flux rope to the complex structure seen in SECCHI HI-1. Many of the differences observed between the corona and heliosphere could be due to viewing geometry, the effects of Thomson scattering, or the different instrument sensitivities. Our approach focuses on converting images from photometric intensity to mass maps. By converting the images to mass maps, we will generate a more qualitative metric of the CME morphology and expansion, including Thomas scattering and instrumental effects.

Using a processing technique to remove the considerable intensities of the F-corona and the stellar field [6], we are able to isolate the brightness of the CME without resorting to a differencing technique that

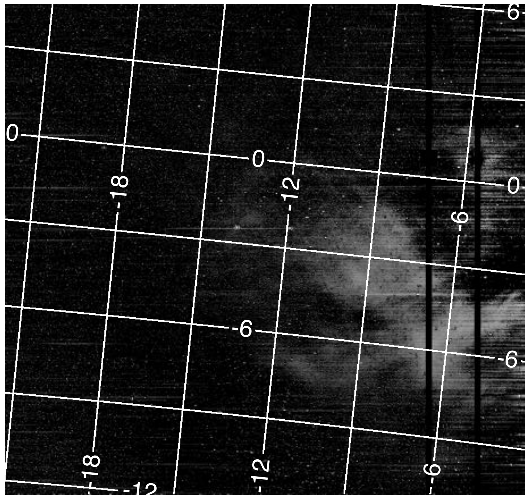

Fig. 3—An image of the 2010-Apr-03 CME from 20:49 UT in HI1-A based on our preliminary background removal techniques. The Helioprojective Coordinate System is overplotted on the data.

could compromise photometry and remove our ability to separate the flux rope structure from the sheath of upstream solar wind material than can be behind a CME driven shock [16].

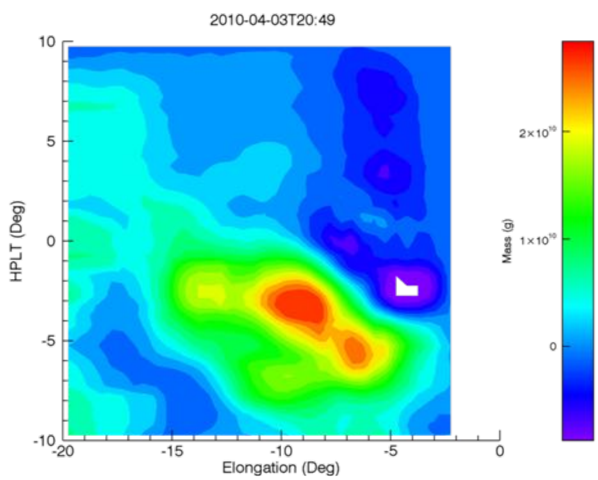

Fig. 4—Contour plot of the mass calculated based on the image from Figure 3. The extra mass in the outer edge of the image is error from the un-shifted background bleeding into the data.

An example image based on our processing is presented in Figure 3. The image clearly still has some streaks and artifacts remaining but clearly isolates the event above the background. Even with this noisy image, we are able to compute the mass map by converting the intensity into density and making some geometric assumptions. The same mass structures are measured features can be tracked across the HI1 FOV.

To demonstrate our image processing, a contour plot of the CME mass is presented in Figure 4. This plot represents the mass along the line of sight of each pixel in the image. These pixels are binned in 1° x 1° to enhance larger features in the contour plot. The boundary between the CME and the background is much clearer in this plot than the raw image. Also, the mass is more heavily concentrated in the back half of the CME, indicating that rather than expanding in a uniform, self-similar fashion, the CME expands more rapidly along the leading edge. This type of expansion could be influenced by the solar wind flowing around CME.

This same data set also allows for the creation of plots along the CME at different times to create simulated *in-situ* plots, along different latitudes or elongations to study how the entire CME structure evolves as a function of radial distance, height or latitude. Figure 5 shows two examples of this, including simulated *in-situ* plots near the CME nose at different heights. These plots show how spacecraft at different locations would see the same event. These plots also can be used, based on the initial increase in mass, the peak in the mass and the eventual drop in mass to determine CME leading edge height, speed, size and expansion.

The right panel of Figure 5 is similar, showing how the mass evolves at different latitudes as the CME expands. The data in this plot demonstrate the decline in the mass at all latitudes as the CME expands as well as the stronger peak mass near the nose.

To validate the photometric consistency of our image processing methods as well as the accuracy of the mass conversion, we examined total masses for 11 different events have been measured based on this same preliminary method in HI1 and compared to the measured masses in COR2 using the technique of Colaninno and Vourlidas [10] and the fitting function from Bein et al. [5].

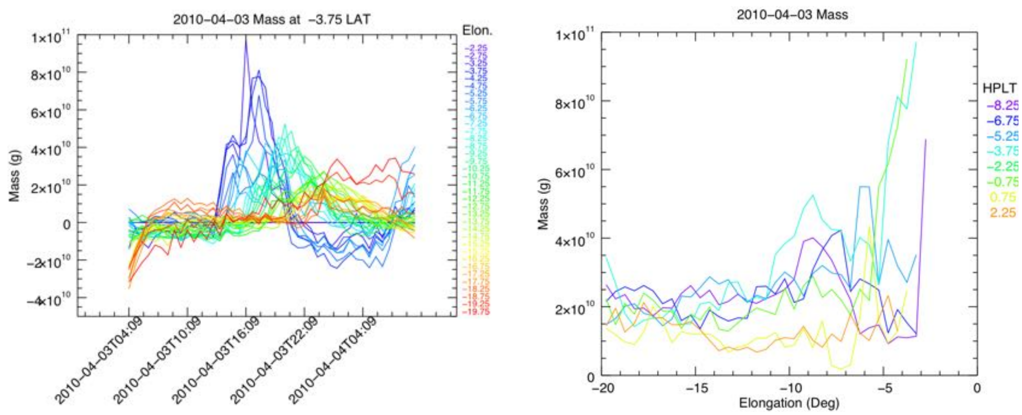

Fig. 5—Left: Each line is a simulated *in-situ* plot of the CME mass at -3.75° (near the CME nose) as the 2010-Apr-03 CME passes at different height. Right: Each line shows the evolution of mass as the CME propagates away from the Sun for a different helioprojective latitude.

The comparison between these masses is presented in Figure 6. The agreement between the two masses is good considering the significant uncertainties inherent in all mass determinations from 2D images. The correlation between the two measurements is 0.37, which jumps to 0.76 if the worst outlier is removed. While the one poor event reveals the need to further validate our technique, the agreement between 91% of our sample indicates the potential ability to determine more accurate masses.

This technique now provides a new method for measuring CME position, speed, density and mass not just as a bulk averaged quantity for the CME as whole, but on a localized scale to show how the mass, and therefore the magnetic field is distributed throughout the body and changes with time. Combined with models of the solar wind, we can now also see how varying upstream parameters influence the different regions of the CME.

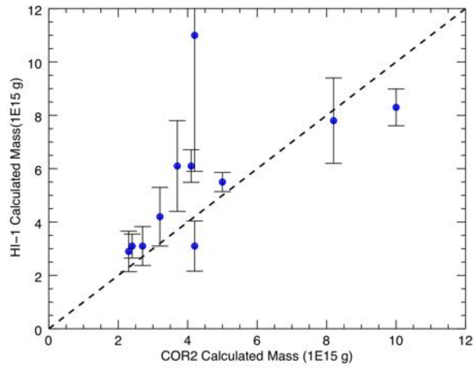

Fig. 6—Comparison between the mass as measured in COR2 and in HI1. The dashed line is the line of unity.

For instance, the CME presented throughout this chapter on April 03, 2010 erupted just to the south of an equatorial coronal hole. This implies that the CME likely encountered a fast speed solar wind stream on it's northward side, but a slow speed stream to the south. The strong density enhancement seen in Figure 4 on the northern end of the rear CME edge could be caused by the compression of fast solar wind as it encounters the CME. Similarly, line plots such as those shown in Figure 5 indicate a CME that is moving in a coherent manner, though the northern region maybe expanding more quickly as it encounter the lower density of a high speed stream.

Now that the processing pipeline has been implemented and the tools are in place. We can begin to analyze more events with a wide range of speeds, masses and upstream solar wind conditions to determine both the coherence of a CME and the degree to which all CMEs may follow the same trends. This will tell us if CMEs are part of a large continuum where each event can be described with a single model, or if there are clear subsets of CMEs that must be modeled differently.

3. UTILIZING A NEW DATA SET: *PSP*-WISPR

3.1 The Wide-Field Imager for Solar Probe

PSP is a unique and unprecedented mission for the heliophysics community. It is structured differently from past missions in that it is not steadily taking data from a consistent distance. Instead the spacecraft is getting progressively closer to the Sun, with an ultimate minimum perihelion of 9.86 $R_{\odot}$. WISPR observes a fixed angular field of view of 13.5° to 108.5° with two detectors, WISPR-I (inner; 13.5°-53°) and WISPR-O (outer; 50.5°-108.5°) and observes the solar corona at lower heights as the mission progresses and the perihelion distance is reduced, allowing for the observation of coronal structures from closer distances than have ever been possible.

Due to the highly elliptical orbit of the spacecraft that is required to reach these low heights, the radial distance of the satellite to the Sun will also change significantly during each individual orbit. Unlike most previous heliospheric observing missions, PSP does not provide continuous observations. Instead, the mission is designed on an encounter basis, taking observations for about 10 days at a time, increasing in cadence as the spacecraft gets closer to perihelion. The first encounter began on 2018 November 01 at 53.8 $R_{\odot}$, with a perihelion on November 05 at 35.6 $R_{\odot}$.

The frequency of CMEs is strongly correlated to the solar cycle ([15] and references therein). At solar maximum, it is common to see multiple CMEs a day erupting from all over the Sun, but at solar minimum there are far fewer eruptions and the CMEs tend to be weaker [51]. Because PSP launched near solar minimum, it was unknown if WISPR would see any CMEs during its initial encounters. Fortunately, a CME entering the inner telescope on the first day of the first encounter was obvious in the images.

The CME persisted long enough in the images that, before performing any detailed analysis on the event, it was clear that this was a slower, less energetic eruption. Given the low speed and the proximity of the event to the streamer that persists in the images throughout the first encounter, this event most likely belongs to the so-called 'streamer blowout' subset of CMEs [48].

Streamer blowouts are a specific classification of events with a unique kinematic profile, featuring a gradual rise phase before the eruption [42], which is an obvious contrast with the faster, more impulsive CMEs that are often associated with flares [55]. These events originate from the streamer belt, but often feature cavities that can be tracked from underneath the streamer until exiting through the streamer cusp [39]. The final speeds of these events tend to reach and stay at the ambient solar wind velocity, so these events are often considered to be tracers of the acceleration and speed of the solar wind [40, 43].

By using the unprecedented observations of WISPR, we can provide another unique constraint on our ability to observe and study CMEs in the heliosphere. For this particular event, this means combining the data with other observations to form as complete a picture as possible for the CME from its eruption and throughout its propagation. The CME in WISPR was also visible in the two LASCO coronagraphs as well as extreme ultraviolet (EUV) data from the Atmospheric Imaging Assembly (AIA [24]) on-board the Solar Dynamics Observatory (SDO). Using all of these data, we can observe the complete evolution of the eruption, from the initial rising of the ejecta in the low corona until it exits the outer WISPR telescope.

3.2 CME in WISPR

As with SECCHI and LASCO data, the WISPR signal is dominated by the F-corona. Unlike those missions due to the rapid movement of the spacecraft, combining many images to determine a stable background will not effectively remove the F-corona in WISPR. Adapting a technique developed by [44] on SECCHI HI-1 data, a background removal technique has been applied to WISPR images allowing for transient K-corona features to be highlighted.

On 2018 November 01, PSP entered its first encounter with the solar corona. This event is presented in detail in [19]. In the first images taken by WISPR during the encounter a streamer was plainly visible in the inner detector close to the solar equatorial plane. This streamer can be seen in each detector in Figure 7. The streamer appears tilted above the mid-plane of the image due only to the pointing and roll of the instrument.

The CME came from the same position angle as the steamer and entered the FOV by 11:15 UT. However, it is not until 12:45 UT that the CME can be clearly distinguished from the streamer cusp. The CME then enters the WISPR-O FOV around 03:45 UT on November 02, growing increasingly faint as it propagates before likely leaving the FOV around 11:15 UT on November 03.

The CME in both detectors is presented in Figure 7. While the CME is difficult to isolate clearly in the outer detector, there are some common characteristics of the event present in each detector. The CME has a strong 'V' shape at the trailing edge. In front of this feature, which is present as a brightness enhancement, there

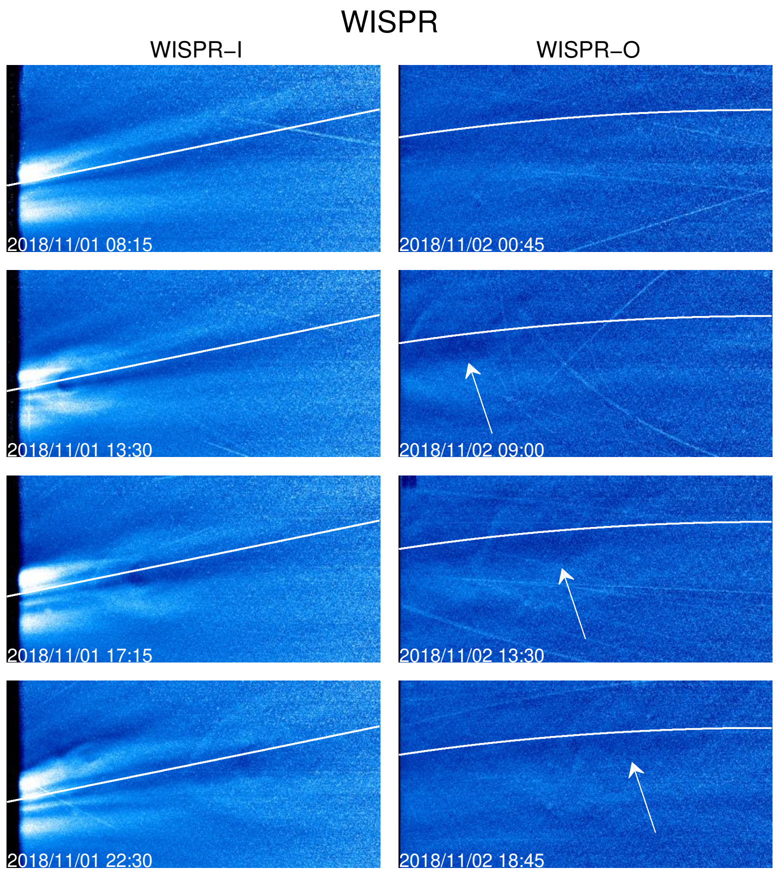

Fig. 7—The CME in both WISPR-I (Left) and WISPR-O (Right). The images from both detectors are cropped to 800x400 pixels. In Detector 2, the white arrows were added to point out where the core of the CME is located. The first image in a each sequence is a pre-event image. The solar equatorial plane has been added as a white line in each image for reference. The bend in the equatorial plane in WISPR-O is a result of the distortion of the detector.

is a coherent circular dark feature. This dark cavity-like structure persists until the CME is no longer visible in WISPR-O.

The CME was faint and relatively slow. Given that the total FOV of WISPR covers about 80 $R_\odot$ (an approximate value, given the changing radial coverage of the instruments as the spacecraft gets closer to the Sun), the CME taking two full days to traverse through the full FOV is indicative of a speed of $\sim$300 km s^{-1}. This low speed, combined with the co-spatial streamer visible in WISPR-I, is further indicative of a steamer blowout.

Figure 8 shows a plot of elongation (angle from the Sun) vs. time (referred to as a J-map [40]) from WISPR observations on 2018 November 01-02, where the elongation is measured in the plane of PSP's orbit. It appears as though the CME is accelerating throughout the FOV of each detector. This is likely an effect of the FOV changing as the radial distance between the spacecraft and the Sun changes during the orbit. At the beginning of the J-map in Figure 8 the spacecraft is 51.6 $R_\odot$ from the Sun and by the end of the J-map, it is

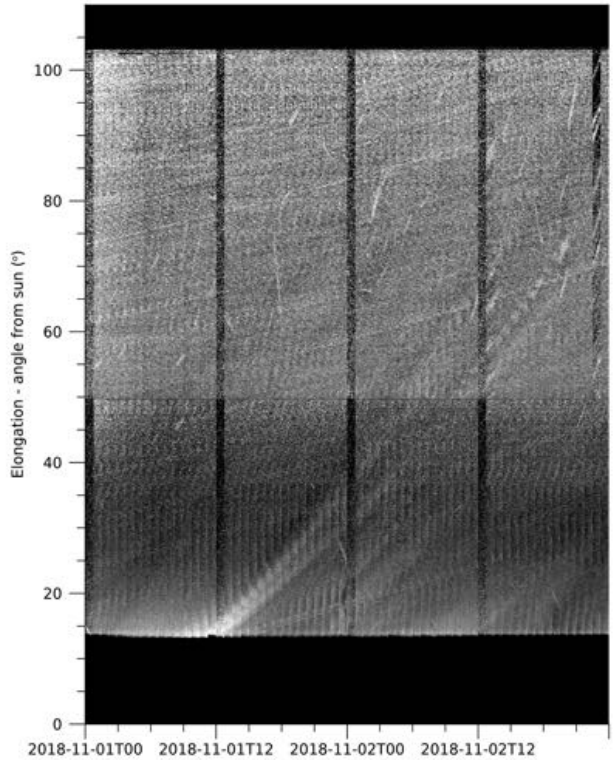

Fig. 8—Height-time plot or J-map of the CME in both WISPR Detectors taken from the spacecraft orbit plane.

at 43.0 $R_{\odot}$. While this change may seem relatively minor, it can have significant impacts on the conversion between elongation and radial distance. Converting 50° elongation on a plane 90° from WISPR into a radial distance, the calculated height reduces by $\sim$10 $R_{\odot}$ from the beginning of Figure 8 to the end.

There is also the possibility that the spacecraft could be getting closer to the CME as it propagates, causing a projection effect that would lead to artificial enhancements to both the bulk and expansion velocities of the CME as the distance between the CME and the satellite decreases. Getting reliable height and velocity measurements from a more stationary instrument is possible and has been done throughout the STEREO mission with various different methods [4, 31]. However, every method does require some simplifications and assumptions, and the extra uncertainties imposed by WISPR make estimating a velocity from J-map significantly more complex [26].

3.3 Comparison with Other Instruments

To confirm the information obtained from the WISPR images the data was compared to that of other instruments to observe the initial eruption and the evolution of the CME. At the time of this eruption, WISPR was about 40° West of the Sun-Earth line and looking back towards the Sun, relative to the Earth. Because of location of the satellite, anything imaged in WISPR was likely to be on the back side of the Sun relative to *STEREO*-A, as the CME was a slow and dim event propagating right behind the occulter, this meant that SECCHI data would not be particularly useful.

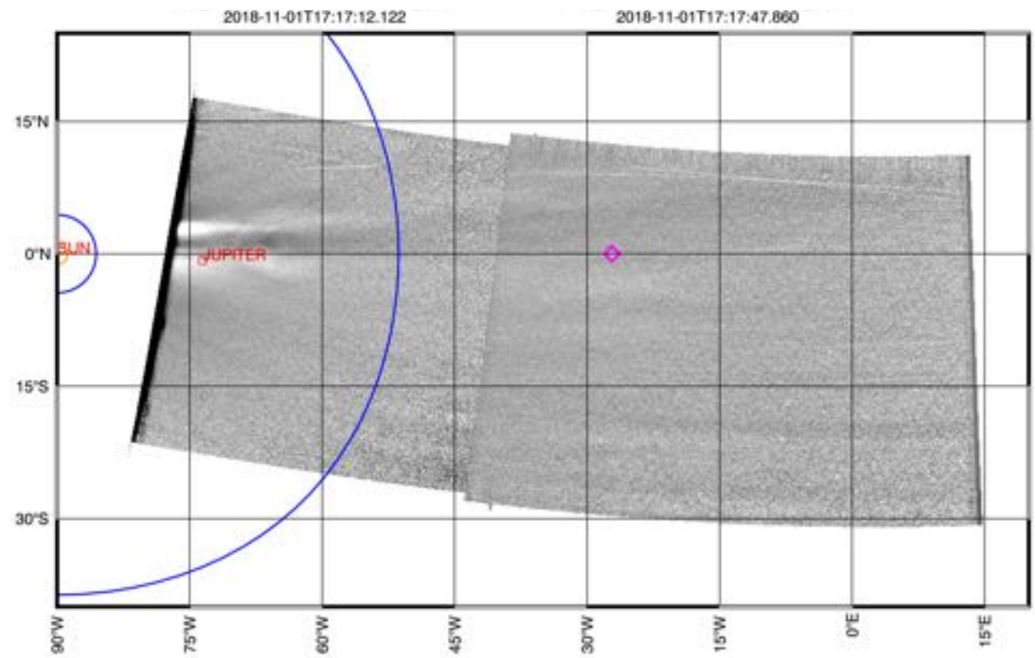

Fig. 9—Observation of the CME in WISPR, in a heliocentric coordinate system with 0° latitude at the PSP orbital plane (see text). The blue circles indicate the approximate position of the C3 field of view based on a projection of the Thomson sphere onto the image plane and ignoring the longitudinal separation of the spacecraft. The pink diamond represents position of the velocity vector of the spacecraft on the image plane. The position of Jupiter is marked as well.

The LASCO coronagraphs, however, are always positioned to observe activity on the western limb of the Sun. Figure 9 compares the WISPR FOV to that of SOHO/LASCO/C3, which is indicated by the blue circle. The C3 field-of-view extends to about 30 $R_\odot$. The pink diamond in Figure 9 shows the direction of PSP's velocity vector at this time. The angle between the directions of the velocity vector and the origin reflects the ellipticity of the PSP orbit; a circular orbit would have the velocity vector perpendicular to the Sun-SC line, e.g., the direction of the line-of-sight at the origin of the PSP orbit plane frame. PSP's orbit plane is Venus' orbital plane (because PSP uses Venus flybys to shrink its orbit), which is inclined by about 3.4° from the solar equatorial plane.

Because the spacecraft are observing from different positions and the range of the WISPR detectors will change as the CME gets closer to the Sun, any attempt to compare the fields of view is just an approximation. However, based on Figure 9, it can be expected that anything that is seen by the inner half of WISPR-I detector while observing close to the western limb should be seen co-temporally in C3.

A few events around the CME were visible in LASCO during the WISPR observations, with one clear choice for a counterpart to the WISPR CME. On November 01, there was a CME observed by C3 that was from a streamer in the solar equatorial plane. This CME was slow, and had a dark, circular cavity in front of a bright trailing edge that came to a cusp at the back end of the CME. A series of snapshots from both LASCO coronagraphs from October 31 through November 02 is shown in Figure 10.

The C3 image taken at 17:16 UT overlaps with the WISPR-I image from Figure 7 taken at 17:15 UT, and the structure looks similar in each detector, though obviously the resolution is better in WISPR. In LASCO,

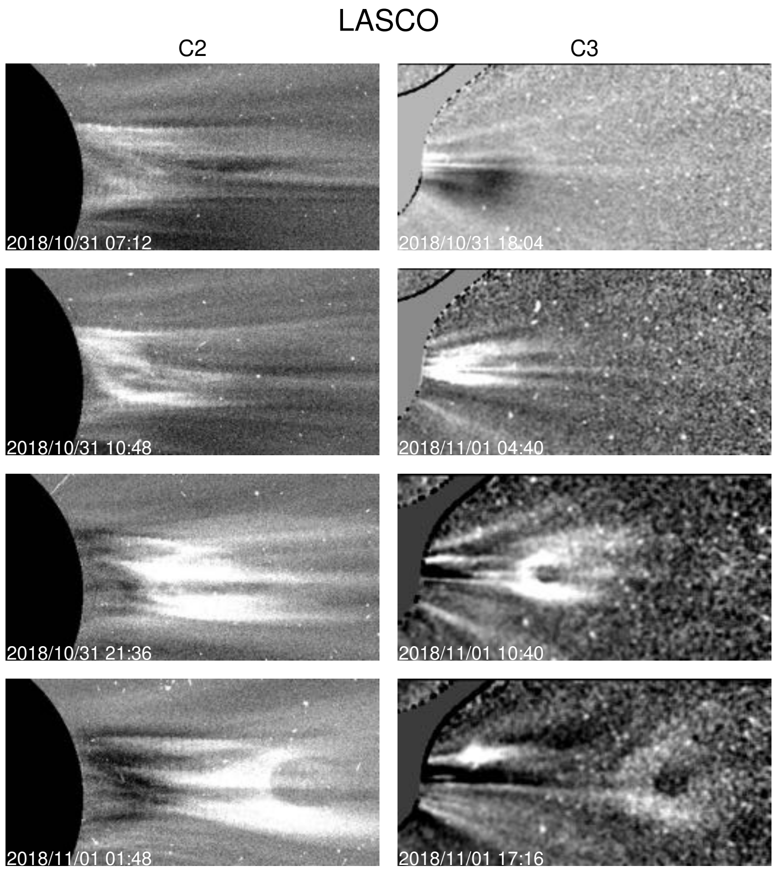

Fig. 10—The CME as observed in LASCO C2 and C3 from the October 31 into November 01. The images from both detectors are cropped to 300x200 pixels. The first frame in each series shows a pre-event image.

the CME appears much more separated from the streamer than at the same time in WISPR, indicating that the part of the streamer that is well observed in WISPR is likely behind the CME and appears close only because of projection effects.

This same CME was also visible in C2. The claw-like structure seen in both WISPR and C3 first becomes visible about halfway through the C2 field of view. Before that, it is difficult to separate the CME from the streamer that is present. As seen in Figure 10 at 10:48 UT on October 31, there does appear to be a a circular, dark feature that could correspond to the cavity observed later. This feature is not radially oriented, and its motion is highly non-radial. This indicates an eruption from a higher latitude being pushed by the overlying magnetic field to the equator until the flux rope reaches the open field lines of the streamer and can then lift off, behavior that was also observed in STEREO [25].

To demonstrate the kinematics of this event, a LASCO J-map is shown in Figure 11. The brightest feature in the J-map corresponds to the trailing edge of the CME, and there is a noticeable expanding, dark feature in front of the trailing edge in C3. The CME rises very gradually between October 31 and November 01, staying within 1° in elongation of the solar surface for nearly 8 hours after the CME first becomes

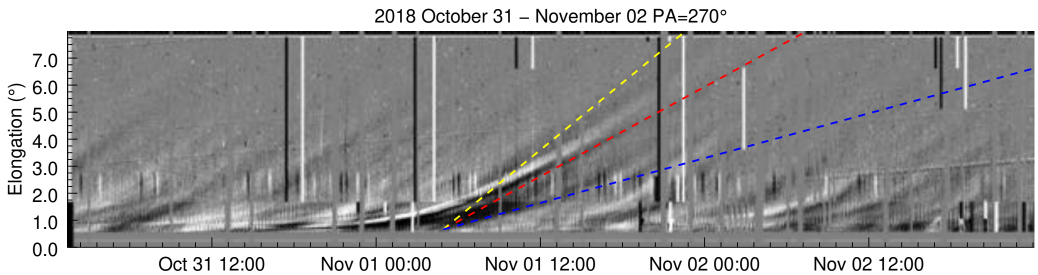

Fig. 11—J-map from LASCO beginning on October 31, combining the C2 and C3 data at position angle 270° (roughly 0° heliographic latitude). The CME is both the bright feature as well as the dark void in front, which correspond to the trailing edge and cavity, respectively. For reference, lines with slopes representing 100 km s^{-1} (blue), 200 km s^{-1} (red) and 300 km s^{-1} (yellow) velocities have been included.

distinguishable in C2. Eventually, the CME picks up speed after it leaves the C2 field of view and propagates approximately linearly through the C3 field of view. The speed determined by a simple estimation of the slope of the density enhancement supports a roughly 300 km s^{-1} velocity for the event.

This approximate result can be confirmed with a more complex kinematic analysis of the bright envelope or claw-like feature, hereafter referred to as the flux rope, and the dark cavity using both WISPR and LASCO. Figure 12 shows the resulting height versus time plots for the flux rope and the dark cavity (right and left panel, respectively). To perform the measurements an ellipse was fit to the outermost edges of the two features that appear in the images. The kinematics are then determined by the temporal evolution of the centroid of the fitted ellipses. The height-time measurements using LASCO images and those made by WISPR observations seem to agree well. The similarity of the images indicate that, despite an angular separation of approximately 40°, the FOVs for WISPR and LASCO overlap and allow for a consistent comparison for this CME.

These plots again show a very slow rise of the CME from the low to the upper corona. The speed of dark cavity is roughly similar with the estimated speed of the flux rope. At 20 $R_{\odot}$ the speed of the dark cavity is estimated to be 285 km s^{-1} and at the same height the flux rope speed of 300 km s^{-1}, based on second order polynomial fits to the height measurements. The acceleration happens in two stages, an initial, low acceleration in the corona before a higher acceleration to a potential slow solar wind speed. Both the cavity and flux rope features undergo the same gradual acceleration profiles around 3.5 km s^{-12}.

On 2018 October 30 at 16:00 UT, a circular cavity was observed at a heliographic latitude of 30° in SDO/AIA. An associated prominence was observed $\sim$37.5 Mm above the solar limb. Around 19:00 UT the cavity started to rise slowly and non-radially, towards the solar equator. Figure 13 shows the eruption of the cavity in different AIA passbands at 21:05 UT. The erupting cavity is observed as a bright blob in AIA 171 Å$\sim$(0.6 MK) and the corresponding feature was observed as dark cavity in the AIA 193 Å (combination of 1.6 MK and 20 MK) passband. The 131 Å (combination of 0.4 MK and 10 MK) passband shows a bright trailing edge with a remarkably similar shape to what is observed in both WISPR and C3. Considering the lack of hot plasma in other wavelengths, it is likely this comes from the cooler ions observed in 131 Å. Also, the corresponding prominence was observed to rise in the cooler AIA passband 304 Å$\sim$(0.05 MK).

The size of the cavity in AIA 193 Å, calculated along the major axis of the feature (see the black line in the top left panel Figure 13), was 59.2 Mm at 21:05 UT. The rising motion of the cavity was slow. To study the

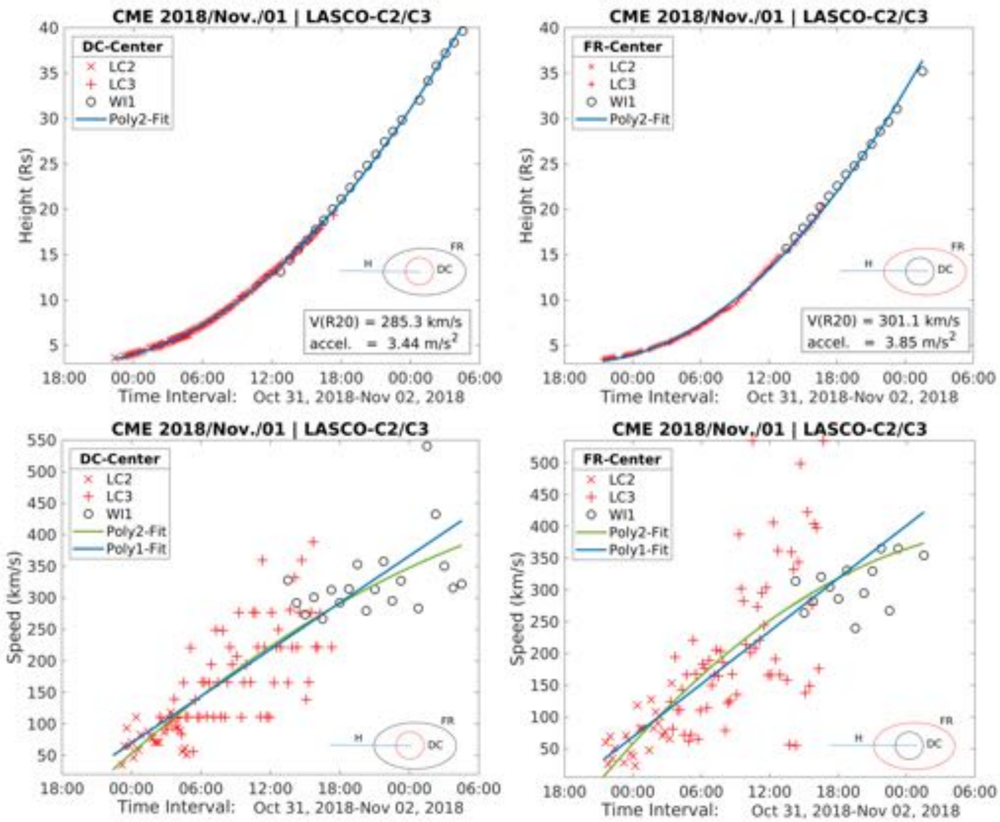

Fig. 12—Top: Kinematics of the cavity (left panel) and flux rope (right panel) from combined observations of WISPR and SOHO/LASCO. In both panels, red and blue markers are used when the features height is determined from LASCO or WISPR images, respectively. A second order polynomial function was used to determine the speed and the acceleration of the cavity and flux rope at 20 $R_{\odot}$. Each feature is measured from its geometric center, based on the circular or elliptical feature as depicted in the schematic at the bottom right corner of the plot. Bottom: Velocity profiles of each feature. The points in these plots are the difference of the height measurements in the top row. The blue line is the analytical derivative of the polynomial fit to the height measurements. The green line is a second order polynomial fit to the velocity points.

rising motion of the erupting cavity quantitatively a slit was made in running difference images from AIA 171 Å to create a height-time plot similar to the white light J-maps (see the Figure 14). The position of the slit is shown by a white line in the lower-left panel of the Figure 13. While the velocity of the leading edge is difficult to determine as it leaves the field of view a few hours after the CME is first visible, the trailing edge can be tracked until the CME completely exits AIA. The rise of the trailing edge of the cavity is shown as red asterisk in the Figure 14. Using a linear fit on the trailing edge, the velocity was determined to be 5.5 km s^{-1} (shown with the green line in Figure 14).

The temperature properties of the erupting cavity were investigated using the differential emission measure (DEM) method by employing the sparse inversion code [9]. Figure 15 shows the emission measure (EM) map at different temperature ranges during the eruption of the cavity. Since the cavity was lifting off very slowly, six AIA passbands (94, 131, 171, 193, 211 and 335 Å) were used in the time range of 20:12 UT to 20:17 UT (selecting the data with minimum noise) to calculate the EM. The EM maps suggest that the temperature of the erupting cavity was $\leqslant$ 1 MK.

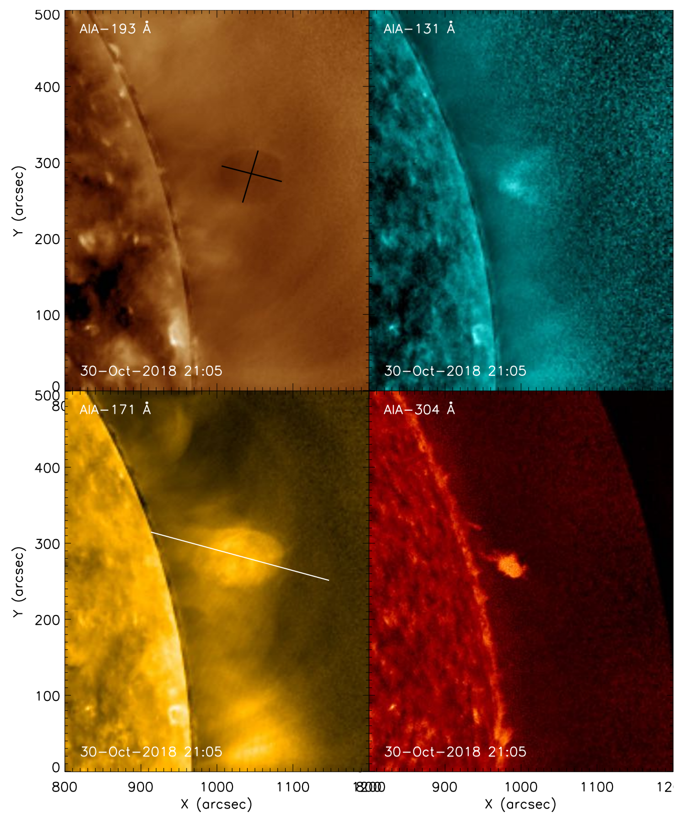

Fig. 13—AIA images during the eruption on October 30. Different wavelengths enhance different elements of the CME including the dark, circular cavity (193 Å; 1.6 MK and 20 MK), the bright trailing edge (131 Å; 0.4 MK and 10 MK), a bright blob that is co-spatial with the cavity (171 Å; 0.6 MK) and the prominence at the base of the eruption (304 Å; 0.05 MK). The black line in the 193 Å frame was used to calculate the size of the cavity. The white line in the 171 Å frame is the approximate direction of motion and was used to measure the height and calculate the velocity of the cavity in AIA.

There is a candidate filament at the proper longitude visible in AIA in the days leading up to the eruption, which is likely the same filament seen to erupt in the 304 Å passband on October 30. It is not immediately apparent what caused the eruption. The filament is still relatively small, and there is nothing in the other wavelengths to indicate a strong eruption.

The lack of a striking low coronal signature is not surprising, considering the speed of the rising motion in AIA is just 5.5 km s^{-1}, there would not likely be a strong flare impulsively providing energy to the CME. Instead this is most likely an eruption of a pre-existing flux rope gradually losing equilibrium, possibly due to a small eruption that is visible just to the south of the cavity in 193 Å in the hours before the eruption. This could have perturbed the overlying field just enough on the southern side to cause the flux rope to begin to rise.

Because the field above the CME would have only been affected on one side, the still-strong magnetic field to the north of the CME deflects the flux rope to the south as it rises, causing the non-radial motion of the CME in AIA. Once the CME reaches the current sheet, it is again deflected, this time radially with the outflowing solar wind. The cavity, maintained by the strength of the magnetic field remains in tact while expanding as the ambient density around it drops.

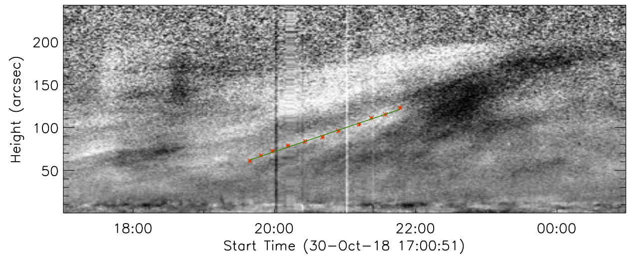

Fig. 14—The height-time plot showing the eruption of the cavity in AIA 171 Å. The position of the slice is shown in the lower-left panel of the Figure 13. The red asterisks mark the positions of the lower edge of the erupting cavity and the linearly fit to the points is in green.

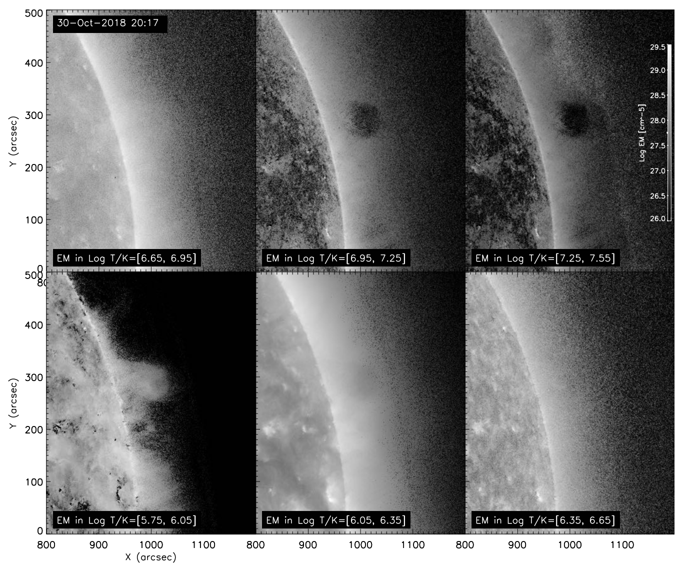

Fig. 15—DEM maps during the eruption of the cavity on 2018 October, 30 at 20:17 UT by the sparse inversion method. Each panel shows the total EM at a different temperature range.

The entire flux rope undergoes a similar expansion, but the brightness at the trailing end of the flux rope remains much much brighter than that of the leading edge throughout the propagation. It is likely that this CME is accelerated by the solar wind, and the compression of plasma on the back of the CME is could why the CME is so much brighter on that side.

3.4 Overall Evolution of the Event

On the first day of the first PSP encounter, WISPR imaged its first CME. By working backwards through multiple data sets in different observers, the entire evolution and morphology of this event can be pieced together. A structure existed in the low corona for an unknown length of time. In hotter wavelengths the structure appears as a cavity while appearing as a density enhancement in the cooler 171 Å images. This indicates a cooler structure, confirmed by DEM analysis that indicates a temperature around 1 MK. At any temperature, the well defined circular structure suggests the structure is likely a flux rope.

Shortly after rotating onto the limb of AIA, something, most likely another nearby, faint eruption, weakens the overlying magnetic field and destabilizes the flux rope, causing it to rise gradually and non-radially toward the equator at a speed around 5.5 km s^{-1}. Over the course of nearly an entire day, the flux rope continues to slowly rise through the C2 field of view before it reaches the open field region and and begins to accelerate before crossing into C3. In the C3 FOV, the acceleration declines until the CME is travelling at a fairly constant speed. The cavity at the center is also still visible, and can be seen to expand as the CME propagates.

Eventually, the CME, including the cavity at the center, enters the WISPR field of view. It propagates directly along the streamer belt lying over the equatorial plane. The J-map made from WISPR data shows signs of an apparent acceleration well into the WISPR-O field of view. It's unlikely that this CME would continue to accelerate at such a large distance, and instead this is most likely the result of the spacecraft getting closer to the CME as it propagates.

A number of factors were aligned for this event to be well observed by multiple satellites. If the CME had gone off just a day earlier or a day later, the cavity would not have rotated onto the limb in AIA to be as clearly observed. LASCO would likewise have most likely missed the cavity and this event would have been just a typical slow streamer blowout.

The observation of this core is extremely valuable, as is the chance to study a flux rope with such a clear structure. Because this CME was not initiated by a large, impulsive energy release manifested as a flare and did not violently exit the corona, there were fewer strong forces contributing to a possible erosion or distortion of the flux rope. Also, because of the relatively weak expansion of the flux rope, the CME structure had a smaller spatial extent in the corona and heliosphere and was therefore less likely to interact with something on its flank (i.e. a streamer). By studying events such as this at a closer range with better resolution, it will be possible to see how a more idealized flux rope propagates through the heliosphere - an important test for theory and models, as is demonstrated in Rouillard et al. [37].

4. CONCLUSIONS

CMEs are complex phenomena. The study of CMEs is often limited by the scope of available data and events. With the launch of new missions, the breadth of data that can be used to observe a CME in the heliosphere has substantially increased. To get the most out of this data and devise a more complete theoretical study of CMEs, it is necessary to challenge the assumptions that were developed with more limited observations to test their validity and see what may be missing.

These assumptions include the idea that a coherent, self-similar structure is an appropriate representation for a CME in the heliosphere. Even if this is true in the low corona where the internal magnetic forces of a CME are dominant, it is unclear how far into the heliosphere this will apply as the CME expands and interacts with the solar wind. If we go into an analysis treating the CME as a consistent, rigid body, we will already be using a tool that is incapable of determining the distinct, non-uniform evolution of the structure and will potentially miss an important piece of the propagation of the CME. This in turn will impose a limit on any future forecasting model.

In chapter 2 we demonstrated the ineffectiveness of geometric models that work in the low corona shortly after the eruption to continue to match observations of the CME as it propagates. This makes any such measurement completely unreliable beyond a few $R_{\odot}$. To obtain useful information about a given event, it is necessary to possess some kind of knowledge of the internal structure of the CME.

Obtaining detailed knowledge of the internal magnetic structure is not possible directly, as we cannot measure the magnetic field of the CME. By converting brightness to mass, which is correlated with the magnetic field strength, we have shown that in a sufficiently well processed image, the CME mass can be isolated from the background signal and the mass can be tracked well into the heliosphere.

With these observations we can determine CME heights along various sections of the CME front as well as observing the degree to which the different sections of the CME are evolving differently, either due to internal forces or interaction the variable upstream solar wind. Our preliminary finding is that CMEs will continue to propagate in bulk as a structurally coherent object and the discrepancies seen in in-situ magnetic field measurements are due to localized variations. In short, while the CME remains a coherent structure, erosion due to interaction with the solar wind will prevent it from being an ideal flux rope.

Prior to *PSP* there was an observational bias towards larger, more impulsive events as these could be better seen from 1 AU. While smaller events could be observed, they were often not resolved to the point where detailed analysis could be performed. However, these smaller eruptions are frequent and make up a large portion of the distribution of all the events flowing out from the Sun. To truly understand the nature of the solar wind and the behavior of all flux ropes within it, detailed study of these smaller events is necessary.

Using WISPR such a study is now possible as demonstrated in Chapter 3. We demonstrate both the better resolution of these events in WISPR as compared to a 1 AU coronagraph as well as the detailed kinematic analysis that WISPR makes possible. Now, instead of focusing our studies on the extreme subset of CME events, we can perform more comprehensive analyses with a more representative sample of events.

We find that, for the first WISPR CME, a strong core at its center indicative of a flux rope, but a more diffuse envelope surrounding that core. This supports the implication of what was seen in chapter 2, where a CME contains a rigid central core that propagates coherently while the outer portions become more chaotic due to interaction with the solar wind. As more events are studied in detail we will better be able to determine if this scenario is applicable to all CMEs regardless of size and speed, or if there are distinct differences in how this evolution unfolds.

Going forward, we will continue to analyze events seen by WISPR. As we approach the upcoming solar maximum, there will hopefully be some larger, impulsive events to compare to past studies as well as more of the small, blowout CMEs for which WISPR is uniquely suited. This will help us determine if CMEs all behave in a similar manner or if there are discrete subsets of CMEs determined by parameters like mass, magnetic field strength and speed.

We will also have data from the SoloHI instrument on-board *Solar Orbiter* to provide another vantage point outside the ecliptic plane. This will help test the coherence of CMEs further by allowing us to image them from a new plane and see the longitudinal evolution of the structure.

We will continue to refine our processing and analysis methods for studying CMEs in the heliosphere to address the questions posed in this work to continue improving forecasting models of space weather at the Earth to prevent disruptions to satellites, radar and radio communications and other systems critical for Naval operations.

ACKNOWLEDGMENTS

This work is the subject one paper published in the Astrophysical Journal Supplemental Series [19] as well as another in preparation. The co-authors include Robin Colaninno, Russell Howard and Guillermo Stenborg of NRL, as well as Alexis Rouillard and Athanasios Kouloumvakos of IRAP, Paullet Liewer of the Jet Propulsion Laboratory and Jie Zhang and Suman Dhakal of George Mason University.

REFERENCES

1. N. Al-Haddad, T. Nieves-Chinchilla, N. P. Savani, N. Lugaz, and I. I. Roussev, "Fitting and Reconstruction of Thirteen Simple Coronal Mass Ejections," *SoPh* **293**(5), 73 (May 2018), doi:10.1007/s11207-018-1288-3.

2. N. Al-Haddad, S. Poedts, I. Roussev, C. J. Farrugia, W. Yu, and N. Lugaz, "The Magnetic Morphology of Magnetic Clouds: Multi-spacecraft Investigation of Twisted and Writhed Coronal Mass Ejections," *ApJ* **870**(2), 100 (Jan 2019), doi:10.3847/1538-4357/aaf38d.

3. T. Amerstorfer, C. Möstl, P. Hess, M. Temmer, M. L. Mays, M. A. Reiss, P. Lowrance, and P. A. Bourdin, "Ensemble Prediction of a Halo Coronal Mass Ejection Using Heliospheric Imagers," *Space Weather* **16**(7), 784–801 (Jul 2018), doi:10.1029/2017SW001786.

4. D. Barnes, J. A. Davies, R. A. Harrison, J. P. Byrne, C. H. Perry, V. Bothmer, J. P. Eastwood, P. T. Gallagher, E. K. J. Kilpua, C. Möstl, L. Rodriguez, A. P. Rouillard, and D. Odstrčil, "CMEs in the Heliosphere: II. A Statistical Analysis of the Kinematic Properties Derived from Single-Spacecraft Geometrical Modelling Techniques Applied to CMEs Detected in the Heliosphere from 2007 to 2017 by STEREO/HI-1," *SoPh* **294**(5), 57 (May 2019), doi:10.1007/s11207-019-1444-4.

5. B. M. Bein, M. Temmer, A. Vourlidas, A. M. Veronig, and D. Utz, "The Height Evolution of the "True" Coronal Mass Ejection Mass derived from STEREO COR1 and COR2 Observations," *ApJ* **768**(1), 31 (May 2013), doi:10.1088/0004-637X/768/1/31.

6. D. Bewsher, D. S. Brown, C. J. Eyles, B. J. Kellett, G. J. White, and B. Swinyard, "Determination of the Photometric Calibration and Large-Scale Flatfield of the STEREO Heliospheric Imagers: I. HI-1," *SoPh* **264**(2), 433–460 (Jul 2010), doi:10.1007/s11207-010-9582-8.

7. G. E. Brueckner, R. A. Howard, M. J. Koomen, C. M. Korendyke, D. J. Michels, J. D. Moses, D. G. Socker, K. P. Dere, P. L. Lamy, and A. Llebaria, "The Large Angle Spectroscopic Coronagraph (LASCO)," *SoPh* **162**(1-2), 357–402 (Dec 1995), doi:10.1007/BF00733434.

8. H. V. Cane and I. G. Richardson, "Interplanetary coronal mass ejections in the near-earth solar wind during 1996–2002," *J. Geophys. Res.* **108(A4)**, 1156, doi:10.1029/2002JA009817 (2003).

9. M. C. M. Cheung, P. Boerner, C. J. Schrijver, P. Testa, F. Chen, H. Peter, and A. Malanushenko, "Thermal Diagnostics with the Atmospheric Imaging Assembly on board the Solar Dynamics Observatory: A Validated Method for Differential Emission Measure Inversions," *ApJ* **807**, 143 (July 2015), doi:10.1088/0004-637X/807/2/143.

10. R. C. Colaninno and A. Vourlidas, "First Determination of the True Mass of Coronal Mass Ejections: A Novel Approach to Using the Two STEREO Viewpoints," *ApJ* **698**, 852–858 (June 2009), doi:10.1088/0004-637X/698/1/852.

11. R. C. Colaninno, A. Vourlidas, and C. C. Wu, "Quantitative comparison of methods for predicting the arrival of coronal mass ejections at Earth based on multiview imaging," *Journal of Geophysical Research (Space Physics)* **118**, 6866–6879 (Nov. 2013), doi:10.1002/2013JA019205.

12. C. E. DeForest, T. A. Howard, and D. J. McComas, "Tracking Coronal Features from the Low Corona to Earth: A Quantitative Analysis of the 2008 December 12 Coronal Mass Ejection," *ApJ* **769**(1), 43 (May 2013), doi:10.1088/0004-637X/769/1/43.

13. N. J. Fox, M. C. Velli, S. D. Bale, R. Decker, A. Driesman, R. A. Howard, J. C. Kasper, J. Kinnison, M. Kusterer, and D. Lario, "The Solar Probe Plus Mission: Humanity's First Visit to Our Star," *SSRv* **204**(1-4), 7–48 (Dec 2016), doi:10.1007/s11214-015-0211-6.

14. J. T. Gosling, S. J. Bame, D. J. McComas, and J. L. Phillips, "Coronal mass ejections and large geomagnetic storms," *Geophys. Res. Lett.* **17**, 901–904 (June 1990).

15. P. Hess and R. C. Colaninno, "Comparing Automatic CME Detections in Multiple LASCO and SECCHI Catalogs," *ApJ* **836**(1), 134 (Feb 2017), doi:10.3847/1538-4357/aa5b85.

16. P. Hess and J. Zhang, "Stereoscopic Study of the Kinematic Evolution of a Coronal Mass Ejection and Its Driven Shock from the Sun to the Earth and the Prediction of Their Arrival Times," *ApJ* **792**, 49 (Sept. 2014), doi:10.1088/0004-637X/792/1/49.

17. P. Hess and J. Zhang, "Predicting CME Ejecta and Sheath Front Arrival at L1 with a Data-Constrained Physical Model," *ApJ* **812**(2), 144 (Oct. 2015), URL `http://stacks.iop.org/0004-637X/812/i=2/a=144`.

18. P. Hess and J. Zhang, "A Study of the Earth-Affecting CMEs of Solar Cycle 24," *SoPh* **292**(6), 80 (Jun 2017), doi:10.1007/s11207-017-1099-y.

19. P. Hess, A. P. Rouillard, A. Kouloumvakos, P. C. Liewer, J. Zhang, S. Dhakal, G. Stenborg, R. C. Colaninno, and R. A. Howard, "WISPR imaging of a pristine CME," *The Astrophysical Journal Supplement Series* **246**(2), 25 (feb 2020), doi:10.3847/1538-4365/ab4ff0, URL `https://doi.org/10.3847%2F1538-4365%2Fab4ff0`.

20. R. A. Howard, J. D. Moses, A. Vourlidas, J. S. Newmark, D. G. Socker, S. P. Plunkett, C. M. Korendyke, J. W. Cook, A. Hurley, and J. M. Davila, "Sun Earth Connection Coronal and Heliospheric Investigation (SECCHI)," *SSRv* **136**(1-4), 67–115 (Apr 2008), doi:10.1007/s11214-008-9341-4.

21. R. A. Howard, A. Vourlidas, V. Bothmer, R. C. Colaninno, C. E. DeForest, B. Gallagher, J. R. Hall, P. Hess, A. K. Higginson, C. M. Korendyke, A. Kouloumvakos, P. L. Lamy, P. C. Liewer, J. Linker, M. Linton, P. Penteado, S. P. Plunkett, N. Poirier, N. E. Raouafi, N. Rich, P. Rochus, A. P. Rouillard, D. G. Socker, G. Stenborg, A. F. Thernisien, and N. M. Viall, "Near-Sun observations of an F-corona decrease and K-corona fine structure," *Nature* **576**, 232–236 (Dec 2019), doi:10.1038/s41586-019-1807-x.

22. T. A. Howard and S. J. Tappin, "Interplanetary Coronal Mass Ejections Observed in the Heliosphere: 1. Review of Theory," *SSRv* **147**(1-2), 31–54 (Oct 2009), doi:10.1007/s11214-009-9542-5.

23. E. K. J. Kilpua, L. K. Jian, Y. Li, J. G. Luhmann, and C. T. Russell, "Multipoint ICME encounters: Pre-STEREO and STEREO observations," *Journal of Atmospheric and Solar-Terrestrial Physics* **73**(10), 1228–1241 (Jun 2011), doi:10.1016/j.jastp.2010.10.012.

24. J. R. Lemen, A. M. Title, D. J. Akin, P. F. Boerner, C. Chou, J. F. Drake, D. W. Duncan, C. G. Edwards, F. M. Friedlaender, and G. F. Heyman, "The Atmospheric Imaging Assembly (AIA) on the Solar Dynamics Observatory (SDO)," *SoPh* **275**(1-2), 17–40 (Jan 2012), doi:10.1007/s11207-011-9776-8.

25. P. Liewer, O. Panasenco, A. Vourlidas, and R. Colaninno, "Observations and Analysis of the Non-Radial Propagation of Coronal Mass Ejections Near the Sun," *SoPh* **290**(11), 3343–3364 (Nov 2015), doi:10.1007/s11207-015-0794-9.

26. P. Liewer, A. Vourlidas, A. Thernisien, J. Qiu, P. Penteado, G. Nisticò, R. Howard, and V. Bothmer, "Simulating White Light Images of Coronal Structures for WISPR/ Parker Solar Probe: Effects of the Near-Sun Elliptical Orbit," *SoPh* **294**(7), 93 (Jul 2019), doi:10.1007/s11207-019-1489-4.

27. N. Lugaz, C. J. Farrugia, R. M. Winslow, N. Al-Haddad, A. B. Galvin, T. Nieves-Chinchilla, C. O. Lee, and M. Janvier, "On the Spatial Coherence of Magnetic Ejecta: Measurements of Coronal Mass Ejections by Multiple Spacecraft Longitudinally Separated by 0.01 au," *ApJL* **864**(1), L7 (Sep 2018), doi:10.3847/2041-8213/aad9f4.

28. R. M. MacQueen, J. A. Eddy, J. T. Gosling, E. Hildner, R. H. Munro, J. Newkirk, G. A., A. I. Poland , and C. L. Ross, "The Outer Solar Corona as Observed from Skylab: Preliminary Results," *ApJL* **187**, L85 (Jan 1974), doi:10.1086/181402.

29. R. M. MacQueen, A. Csoeke-Poeckh, E. Hildner, L. House, R. Reynolds, A. Stanger, H. Tepoel, and W. Wagner, "The High Altitude Observatory coronagraph/polarimeter on the Solar Maximum Mission.," *SoPh* **65**(1), 91–107 (Feb 1980), doi:10.1007/BF00151386.

30. M. L. Mays, A. Taktakishvili, A. Pulkkinen, P. J. MacNeice, L. Rastätter, D. Odstrcil, L. K. Jian, I. G. Richardson, J. A. LaSota, and Y. Zheng, "Ensemble Modeling of CMEs Using the WSA-ENLIL+Cone Model," *SoPh* **290**(6), 1775–1814 (Jun 2015), doi:10.1007/s11207-015-0692-1.

31. W. Mishra, N. Srivastava, and J. A. Davies, "A Comparison of Reconstruction Methods for the Estimation of Coronal Mass Ejections Kinematics Based on SECCHI/HI Observations," *ApJ* **784**(2), 135 (Apr 2014), doi:10.1088/0004-637X/784/2/135.

32. M. J. Owens, M. Lockwood, and L. A. Barnard, "Coronal mass ejections are not coherent magnetohydrodynamic structures," *Scientific Reports* **7**, 4152 (Jun 2017), doi:10.1038/s41598-017-04546-3.

33. E. Palmerio, C. Scolini, D. Barnes, J. Magdalenić, M. J. West, A. N. Zhukov, L. Rodriguez, M. Mierla, S. W. Good, and D. E. Morosan, "Multipoint Study of Successive Coronal Mass Ejections Driving Moderate Disturbances at 1 au," *ApJ* **878**(1), 37 (Jun 2019), doi:10.3847/1538-4357/ab1850.

34. W. Poomvises, J. Zhang, and O. Olmedo, "Coronal Mass Ejection Propagation and Expansion in Three-dimensional Space in the Heliosphere Based on Stereo/SECCHI Observations," *ApJL* **717**, L159–L163 (July 2010), doi:10.1088/2041-8205/717/2/L159.

35. P. Riley and N. U. Crooker, "Kinematic Treatment of Coronal Mass Ejection Evolution in the Solar Wind," *ApJ* **600**(2), 1035–1042 (Jan 2004), doi:10.1086/379974.

36. P. Riley, M. L. Mays, J. Andries, T. Amerstorfer, D. Biesecker, V. Delouille, M. Dumbović, X. Feng, E. Henley, J. A. Linker, C. Möstl, M. Nuñez, V. Pizzo, M. Temmer, W. K. Tobiska, C. Verbeke, M. J. West, and X. Zhao, "Forecasting the Arrival Time of Coronal Mass Ejections: Analysis of the CCMC CME Scoreboard," *Space Weather* **16**(9), 1245–1260 (Sep 2018), doi:10.1029/2018SW001962.

37. A. Rouillard, N. Poirier, M. Lavarra, A. Bourdelle, A. Kouloumvakos, A. Vourlidas, K. V., P. Hess, P. Liewer, R. Howard, G. Stenborg, and R. N., "Modelling the early evolution of a small Coronal Mass Ejection imaged by Parker Solar Probe.," *ApJS* (2020).

38. N. R. Sheeley, D. J. Michels, R. A. Howard, and M. J. Koomen, "Initial observations with the SOLWIND coronagraph," *ApJL* **237**, L99–L101 (May 1980), doi:10.1086/183243.

39. N. R. Sheeley, Y. M. Wang, S. H. Hawley, G. E. Brueckner, K. P. Dere, R. A. Howard, M. J. Koomen, C. M. Korendyke, D. J. Michels, and S. E. Paswaters, "Measurements of Flow Speeds in the Corona Between 2 and 30 $R_\odot$," *ApJ* **484**(1), 472–478 (Jul 1997), doi:10.1086/304338.

40. N. R. Sheeley, J. H. Walters, Y. M. Wang, and R. A. Howard, "Continuous tracking of coronal outflows: Two kinds of coronal mass ejections," *J. Geophys. Res.* **104**(A11), 24739–24768 (Nov 1999), doi:10.1029/1999JA900308.

41. T. Singh, M. S. Yalim, and N. V. Pogorelov, "A Data-constrained Model for Coronal Mass Ejections Using the Graduated Cylindrical Shell Method," *ApJ* **864**(1), 18 (Sep 2018), doi:10.3847/1538-4357/aad3b4.

42. N. Srivastava, R. Schwenn, B. Inhester, G. Stenborg, and B. Podlipnik, "Acceleration Profile of the Slow Solar Wind as Inferred from Gradual Mass Ejections Observed by LASCO," *SSRv* **87**, 303–306 (Jan 1999), doi:10.1023/A:1005189610536.

43. N. Srivastava, R. Schwenn, B. Inhester, S. F. Martin, and Y. Hanaoka, "Factors Related to the Origin of a Gradual Coronal Mass Ejection Associated with an Eruptive Prominence on 1998 June 21-22," *ApJ* **534**(1), 468–481 (May 2000), doi:10.1086/308749.

44. G. Stenborg, R. A. Howard, and J. R. Stauffer, "Characterization of the White-light Brightness of the F-corona between 5° and 24° Elongation," *ApJ* **862**(2), 168 (Aug 2018), doi:10.3847/1538-4357/aacea3.

45. A. Thernisien, A. Vourlidas, and R. A. Howard, "Forward Modeling of Coronal Mass Ejections Using STEREO/SECCHI Data," *SoPh* **256**, 111–130 (May 2009), doi:10.1007/s11207-009-9346-5.

46. A. F. R. Thernisien, R. A. Howard, and A. Vourlidas, "Modeling of Flux Rope Coronal Mass Ejections," *ApJ* **652**, 763–773 (Nov. 2006), doi:10.1086/508254.

47. R. Tousey, J. D. F. Bartoe, J. D. Bohlin, G. E. Brueckner, J. D. Purcell, V. E. Scherrer, J. Sheeley, N. R., R. J. Schumacher, and M. E. Vanhoosier, "A Preliminary Study of the Extreme Ultraviolet Spectroheliograms from Skylab," *SoPh* **33**(2), 265–280 (Dec 1973), doi:10.1007/BF00152418.

48. A. Vourlidas and D. F. Webb, "Streamer-blowout Coronal Mass Ejections: Their Properties and Relation to the Coronal Magnetic Field Structure," *ApJ* **861**(2), 103 (Jul 2018), doi:10.3847/1538-4357/aaca3e.

49. A. Vourlidas, B. J. Lynch, R. A. Howard, and Y. Li, "How Many CMEs Have Flux Ropes? Deciphering the Signatures of Shocks, Flux Ropes, and Prominences in Coronagraph Observations of CMEs," *SoPh* **284**, 179–201 (May 2013), doi:10.1007/s11207-012-0084-8.

50. A. Vourlidas, R. A. Howard, S. P. Plunkett, C. M. Korendyke, A. F. R. Thernisien, D. Wang, N. Rich, M. T. Carter, D. H. Chua, and D. G. Socker, "The Wide-Field Imager for Solar Probe Plus (WISPR)," *SSRv* **204**(1-4), 83–130 (Dec 2016), doi:10.1007/s11214-014-0114-y.

51. D. F. Webb and R. A. Howard, "The solar cycle variation of coronal mass ejections and the solar wind mass flux," *J. Geophys. Res.* **99**(A3), 4201–4220 (Mar 1994), doi:10.1029/93JA02742.

52. D. F. Webb and T. A. Howard, "Coronal Mass Ejections: Observations," *Living Reviews in Solar Physics* **9**(1), 3 (Jun 2012), doi:10.12942/lrsp-2012-3.

53. A. M. Wold, M. L. Mays, A. r. Taktakishvili, L. K. Jian, D. Odstrcil, and P. MacNeice, "Verification of real-time WSA-ENLIL+Cone simulations of CME arrival-time at the CCMC from 2010 to 2016," *Journal of Space Weather and Space Climate* **8**, A17 (Mar 2018), doi:10.1051/swsc/2018005.

54. B. E. Wood and R. A. Howard, "An Empirical Reconstruction of the 2008 April 26 Coronal Mass Ejection," *ApJ* **702**(2), 901–910 (Sep 2009), doi:10.1088/0004-637X/702/2/901.

55. J. Zhang, K. P. Dere, R. A. Howard, and A. Vourlidas, "A Study of the Kinematic Evolution of Coronal Mass Ejections," *ApJ* **604**(1), 420–432 (Mar 2004), doi:10.1086/381725.

56. J. Zhang, P. Hess, and W. Poomvises, "A Comparative Study of Coronal Mass Ejections with and Without Magnetic Cloud Structure near the Earth: Are All Interplanetary CMEs Flux Ropes?," *SoPh* **284**, 89–104 (May 2013), doi:10.1007/s11207-013-0242-7.